Low-order modeling for transition prediction applicable to wind-turbine rotors

Thales Fava[1], Mikaela Lokatt[1], Niels Sørensen[2], Frederik Zahle[2], Ardeshir Hanifi[1], and Dan Henningson[1]

[1]Department of Mechanics, Linné FLOW Centre, SeRC, KTH Royal Institute of Technology, Stockholm, Sweden
[2]Department of Wind Energy, Technical University of Denmark, Risø Campus, Roskilde, Denmark

Correspondence: Thales Fava (fava@kth.se)

Abstract.

This work aims at developing a low-order framework to predict the onset of transition over wind-turbine blades without requiring three-dimensional simulations. The effects of three-dimensionality and rotation on the transition location are also analyzed. The framework consists of a model to approximate the base-flow and another to predict the transition location. The

5 former is based on the quasi-three-dimensional Euler and boundary-layer equations and only requires the pressure distribution over an airfoil to provide an approximation for the base-flow over the blade. The latter is based on the envelope of N factors method, where this quantity is computed using the parabolized stability equations (PSE) considering rotational effects. It is shown that rotation accelerates the flow towards the tip of the blade in the fully developed flow region and towards the opposite direction close to the stagnation point. The database method embedded in the EllipSys3D RANS code indicates overly

10 premature transition locations, matching those obtained with a PSE analysis of a two-dimensional base-flow. The consideration of the spanwise velocity, as carried out in the developed model, has a stabilizing effect, delaying transition. Conversely, rotation plays a destabilizing role, hastening the transition onset. Moreover, airfoils with lower pressure gradients are more susceptible to its effects. The increase in the rotation speed makes transition occur through increasingly oblique disturbances from the middle to the tip of the blade, whereas the opposite happens for lower radial positions. Tollmien-Schlichting (TS) waves seem

15 to trigger transition. However, highly oblique critical modes that may be intermediates between TS and crossflow ones occur for low radii. The developed framework allows transition prediction with reasonable accuracy using chordwise c_p distributions as input, such as those provided by XFOIL.

1 Introduction

In wind-turbine design, accurate determination of aerodynamic loads is of importance as they are related to properties, such as

20 performance and structural loads. Since the aerodynamic loads can be influenced by the boundary-layer character, an accurate determination of the transition location can be significant to obtain a successful wind-turbine design. This has long been recognized by aerodynamiscists, and significant efforts have been devoted to the development of transition models (Saric et al., 2003; Langtry et al., 2006; Pasquale et al., 2009; Krumbein, 2009; Colonia et al., 2017).

A number of models based on the transport equations, such as the γ equation model (Colonia et al., 2017) and the $\gamma - \tilde{Re}_{\Theta}$

25   equation model (Menter et al., 2006; Langtry et al., 2006; Sørensen, 2009; Menter et al., 2015; Langtry et al., 2015), as well as those based on stability analysis, such as the envelope e^N model (van Ingen, 2008), are available for transition prediction. These models are compatible with modern RANS-based, CFD solvers, and they can provide transition predictions at a relatively low computational cost. As such, they are common in engineering applications. While their accuracy has been validated for several two- and three-dimensional flow cases, additional knowledge about their performance for rotating wind-turbine blades would

30   likely be beneficial.

There are also more detailed models, such as those based on direct numerical simulations (DNS) and parabolized stability equations (PSE) (Saric et al., 2003; Pasquale et al., 2009), which can provide accurate transition prediction for complex three-dimensional flow cases. DNS aims at exactly resolving the flow field, and it can thus provide detailed information about velocity fluctuations within the boundary layer, based on which information about transition and turbulence characteristics can

35   be derived. PSE models compute the growth of disturbance waves within a given boundary layer. They are thus related to envelope e^N methods, which compute an envelope for the growth rate for a set of disturbance waves. In two-dimensional flow fields, the waves are typically of the Tollmien-Schlichting type (van Ingen, 2008), whereas in three-dimensional flow fields, waves of cross-flow type are also common (Saric et al., 2003). DNS and PSE models commonly have a high computational cost. They are thus not very well-suited for wind-turbine design applications that involve analyses of a large number of different

40   design configurations and flow cases.

The present work aims to develop a low-order model for transition prediction applicable to wind-turbine blades and understand the effects of three-dimensionality and rotation for two specific wind-turbine rotors. Firstly, a model to generate an approximation for the boundary-layer profiles over wind-turbine blades is developed. This model is based on the boundary-layer equations (BLE) and accounts for both rotational and quasi-three-dimensional effects. A technique to obtain an approximation

45   for the spanwise velocity is also provided, such that the only required external inputs to the BLE are the chordwise distribution of pressure or streamwise velocity, like that provided by XFOIL (Drela, 1989), and the blade geometry. Secondly, the method of the envelope of N factors is employed to predict the transition locations. The N factors are obtained using an existing PSE code (Hanifi et al., 1994) to which rotation effects are added. The developed framework is applied to two different full-scale wind-turbine geometries, and the results are compared with base-flow and transition data from EllipSys3D RANS simulations

50   (Michelsen, 1992, 1994; Sørensen, 1994, 2009). Transition locations provided by this solver rely on a database method, which has a restricted accuracy range. Therefore, the PSE results for the transition characteristics can also indicate the accuracy of the RANS predictions. Finally, the effects of the variation of the rotation speed and spanwise velocity on the transition locations are analyzed, and the suitability of XFOIL results as input to the developed model is assessed.

2   Boundary-layer model

55   This section describes the boundary-layer (BL) model developed in this work.

WIND
ENERGY
SCIENCE
DISCUSSIONS

2.1 Coordinate system

The coordinate system employed in the BL model is illustrated in Fig. 1. The blade rotates around a vertical axis at a constant angular velocity ω, and the coordinate system follows the wing model in its rotation. Therefore, centrifugal and Coriolis forces need to be included in the fluid-dynamic equations (Kundu et al., 2016). The first coordinate direction x_1 follows the wing

60　contour along a circular arc with radius r_0, the second coordinate direction x_2 is perpendicular to the x_1 direction in the plane tangent to the wing surface, whereas the third coordinate direction x_3 is defined to be in the direction normal to the surface. Hence, x_1, x_2, x_3 describe an orthogonal, curvilinear coordinate system. The error committed by assuming that the x_1 and x_2 directions are respectively the streamwise and spanwise directions is low. That is because the chord to radius ratio and the sweep angle are small in the analyzed wind-turbine blades. For instance, the angle between the x_2 and spanwise directions
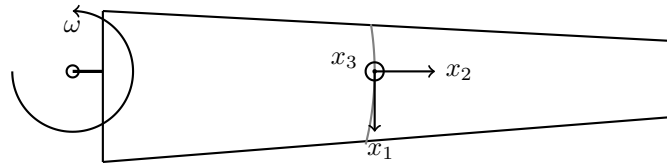
65　oscillates between $1°$ and $4°$.

Figure 1. Coordinate system.

2.1.1 Boundary-layer equations

There are several integral formulations of the boundary-layer equations (BLE) (Du and Selig, 2000; van Garrel, 2004; Dumitrescu and Cardos, 2011; Drela, 2013; Garcia et al., 2014). However, a differential formulation is expected to be more accurate than its integral counterpart, and, based on experience, it appears that an accurate base-flow is needed to obtain correct

70　results in a subsequent stability analysis. For this reason, a differential formulation is chosen in the present case.

When expressed in the coordinate system described in Sect. (2.1), the differential form of the BLE can be written as (Warsi, 1999; Schlichting and Gersten, 2017)

$$\frac{\partial}{\partial x_1}\left(\rho h_2 h_3 u_1\right) + \frac{\partial}{\partial x_2}\left(\rho h_1 h_3 u_2\right) + \frac{\partial}{\partial x_3}\left(\rho h_1 h_2 u_3\right) = 0, \tag{1}$$

$$\rho\left(\frac{u_1}{h_1}\frac{\partial u_1}{\partial x_1} + \frac{u_2}{h_2}\frac{\partial u_1}{\partial x_2} + \frac{u_3}{h_3}\frac{\partial u_1}{\partial x_3} + \frac{1}{h_1 h_2}\left(\frac{\partial h_1}{\partial x_2}u_1 u_2 - \frac{\partial h_2}{\partial x_1}u_2^2\right)\right) = \tag{2}$$

75

$$-\frac{1}{h_1}\frac{\partial p}{\partial x_1} + \frac{1}{Re}\frac{1}{h_3}\frac{\partial}{\partial x_3}\left(\frac{\mu}{h_3}\frac{\partial u_1}{\partial x_3}\right) + \rho\left(2\Omega_3 u_2 + \frac{\Omega^2}{2h_1}\frac{\partial r^2}{\partial x_1}\right),$$

$$\rho \left(\frac{u_1}{h_1} \frac{\partial u_2}{\partial x_1} + \frac{u_2}{h_2} \frac{\partial u_2}{\partial x_2} + \frac{u_3}{h_3} \frac{\partial u_2}{\partial x_3} + \frac{1}{h_1 h_2} \left(\frac{\partial h_2}{\partial x_1} u_1 u_2 - \frac{\partial h_1}{\partial x_2} u_1^2 \right) \right) = \tag{3}$$

$$- \frac{1}{h_2} \frac{\partial p}{\partial x_2} + \frac{1}{Re} \frac{1}{h_3} \frac{\partial}{\partial x_3} \left(\frac{\mu}{h_3} \frac{\partial u_2}{\partial x_3} \right) + \rho \left(-2\Omega_3 u_1 + \frac{\Omega^2}{2h_2} \frac{\partial r^2}{\partial x_2} \right),$$

80

$$\rho c_p \left(\frac{u_1}{h_1} \frac{\partial T}{\partial x_1} + \frac{u_2}{h_2} \frac{\partial T}{\partial x_2} + \frac{u_3}{h_3} \frac{\partial T}{\partial x_3} \right) = \frac{1}{RePr} \frac{1}{h_3} \frac{\partial}{\partial x_3} \left(\frac{\kappa}{h_3} \frac{\partial T}{\partial x_3} \right) + \tag{4}$$

$$(\gamma - 1) M^2 \left\{ \frac{u_1}{h_1} \frac{\partial p}{\partial x_1} + \frac{u_2}{h_2} \frac{\partial p}{\partial x_2} + \frac{\mu}{Re} \left[\left(\frac{\partial u_1}{\partial x_3} \right)^2 + \left(\frac{\partial u_2}{\partial x_3} \right)^2 \right] \right\}.$$

In these equations, $c_p, \gamma, \kappa, \mu, M, Re$, and Pr denote specific heat capacity at constant pressure, ratio of specific heats, thermal conductivity, dynamic viscosity, Mach number, Reynolds number based on a reference length l_0, and Prandtl number, respectively. Moreover, ρ, p, and T denote density, pressure, and temperature, whereas $\mathbf{u}, \boldsymbol{\Omega}$, and $\mathbf{h}$ represent velocity, rotation,

85 and metric vectors, respectively. The subscripts 1, 2, and 3 indicate components in the respective x_1, x_2, and x_3 directions. r is the radial position.

In the BL model, the chordwise curvature of the wing model is neglected, while the radial curvature is considered. Thus, the metric vector becomes

$$h_1 = \frac{x_2 + r_0}{r_0}, \quad h_2 = 1, \quad h_3 = 1. \tag{5}$$

90 Since the code is intended for analysis of laminar flows, turbulent fluctuations and statistics need not be considered. In order to obtain a well-conditioned system which solution is compatible with the subsequent PSE analysis, the terms in the system of Eqs. (1) to (4) are normalized by the reference quantities given in Table 1. The value of l_0 is set to c_0, the chord of the airfoil at the radial position r_0, where the analysis is performed.

2.1.2 Spanwise-derivative approximations

95 As they stand, the BL equations are dependent on all three coordinate directions so that their numerical solution requires a full volume discretization. Such a discretization can easily result in a solution procedure that is very costly from a computational perspective. By employing approximate models for the derivative terms in the x_2 direction, instead of exact expressions, one can obtain a quasi-three-dimensional model requiring discretization in the x_1 and x_3 directions only. The reduced dimension of the discretization typically results in significant savings in computational cost and meshing effort. Furthermore, a judicious

100 selection of the model for the x_2 derivative can provide accurate base-flows. These beneficial properties lead a quasi-three-dimensional model to be employed in the present work.

Table 1. Reference nondimensionalization values. ∞ denotes freestream values.

Variable	Nondimensionalization value
Length in the streamwise (x_1) direction	l_0
Length in the normal (x_3) direction	$\left(\frac{\mu_\infty x_1}{\rho_\infty u_\infty}\right)^{\frac{1}{2}}$
Velocity	u_∞
Angular velocity	$\frac{u_\infty}{l_0}$
Density	ρ_∞
Pressure	p_∞
Temperature	T_∞
Dynamic viscosity	μ_∞
Thermal conductivity	κ_∞

Similarity solutions for rotating flows suggest that the velocity in the x_1 direction can be assumed to depend on the x_2 coordinate linearly (Greenspan, 1968; Hernandez, 2011). This approximation is employed in the present work, together with the further assumption that the velocity in the x_2 direction, pressure, and temperature does not depend on x_2. Thus,

105

$$u_1 = u_{1_0}\frac{x_2 + r_0}{r_0}, \quad u_2 = u_{2_0}, \quad p = p_0, \quad T = T_0. \tag{6}$$

The subscript 0 denotes evaluation at the radial location r_0. This choice can result in a momentum imbalance in the x_2 direction at the boundary-layer edge, as pointed by Sturdza (2003) for swept-wing flows. Sturdza argued that the imbalance could be compensated by defining an additional source term A that accounts for the momentum difference. The extra source term is then multiplied by a blending function $f(x_3)$ and added to the right-hand side of the spanwise momentum equation (Eq.

110 (3)). A is found by considering momentum balance at the boundary-layer edge. With the current approximation of spanwise derivatives and curvature terms, A becomes

$$A = \rho u_{1_e}\frac{\partial u_{2_e}}{\partial x_1} - \frac{\rho u_{1_e}^2}{r_0} - \rho\left(-2\Omega_3 u_1 + \Omega^2 r_0\right), \tag{7}$$

where the subscript e denotes evaluation at the boundary-layer edge. The blending function is selected to linearly depend on the wall-normal distance inside the boundary layer, i.e.,

115

$$f(x_3) = \frac{x_3}{x_{3_e}}. \tag{8}$$

5

2.1.3 Discretization and solution

The spanwise approximations described in Sect. (2.1.2) make the system of the BLE (Eqs. (1) to (4)) include only derivatives in the x_1 and x_3 directions. The derivatives in the x_3 direction are evaluated using a second-order central finite-difference scheme, whereas the derivatives in the x_1 direction are evaluated using a second-order backward Euler finite-difference scheme.

120   The BLE can be expressed as

$$\mathbf{A_1}\boldsymbol{\Phi} + \mathbf{A_2}\frac{\partial \boldsymbol{\Phi}}{\partial x_3} + \mathbf{A_3}\frac{\partial^2 \boldsymbol{\Phi}}{\partial x_3^2} + \mathbf{A_4}\frac{\partial \boldsymbol{\Phi}}{\partial x_1} = \mathbf{A_5}, \tag{9}$$

where $\boldsymbol{\Phi} = (u_1, u_2, T)^T$ denotes the vector of primary variables. Pressure can be obtained from those variables by using the constitutive relations for isentropic flow. The components of the matrices $\mathbf{A_1}, \mathbf{A_2}, \mathbf{A_3}, \mathbf{A_4}$, and $\mathbf{A_5}$ are found by collecting terms in Eqs. (1) to (4).

125   The solution is computed by space marching in the x_1 direction. Uniform boundary conditions are assumed at the inflow. The attachment-line equations (Cebeci, 1999) are solved at the first inflow node, since the BLE are ill-conditioned when u_1 is equal to zero. Because of the boundary-layer singularity (Goldstein, 1948), the system of equations can become strongly ill-conditioned if flow separation is encountered. However, the present code is intended to be used for transition prediction, and separation within a laminar-flow region typically causes transition. Therefore, the separation point can be taken as a reasonable

130   approximation of the transition location, and the issue is circumvented.

2.2 Edge velocity model

The velocity in the x_2 direction at the boundary-layer edge is required as input to the quasi-three-dimensional BL model. In order to avoid the necessity of a costly simulation to obtain it, a model for u_{2_e} is devised with inspiration from the conical-wing approximation (Cebeci, 1999; Sturdza, 2003) . An approximation for u_{2_e} is obtained by combining the Euler equation in the

135   x_2 direction with an approximation for the variation of the pressure coefficient in this direction. The Euler equation in the x_2 direction can be written as (Warsi, 1999)

$$\rho\left[\frac{u_1}{h_1}\frac{\partial u_2}{\partial x_1} + \frac{u_2}{h_2}\frac{\partial u_2}{\partial x_2} + \frac{u_3}{h_3}\frac{\partial u_2}{\partial x_3} + \frac{1}{h_1 h_2}\left(\frac{\partial h_2}{\partial x_1}u_1 u_2 - \frac{\partial h_1}{\partial x_2}u_1^2\right) + \frac{1}{h_2 h_3}\left(\frac{\partial h_2}{\partial x_3}u_2 u_3 - \frac{\partial h_3}{\partial x_2}u_3^2\right)\right] = -\frac{1}{h_2}\frac{\partial p}{\partial x_2} + F_{rot_2}, \tag{10}$$

where

$$F_{rot_2} = \rho\left[2u_3\Omega_1 - 2u_1\Omega_3 - (\Omega_2 x_3 - \Omega_3 x_2)\Omega_3 + (\Omega_1 x_2 - \Omega_2 x_1)\Omega_1\right]. \tag{11}$$

140   We assume that $\frac{u_2}{h_2}\frac{\partial u_2}{\partial x_2} \approx 0$, based on the fact that the flow and the variations in the x_2 direction have a small magnitude. A second hypothesis is that $\frac{u_3}{h_3}\frac{\partial u_2}{\partial x_3} \approx 0$, built on the evidence that the flow and variations in the normal direction at the boundary-layer edge are small. Since $u_3 \approx 0$ and $\Omega_1 \approx 0$, the term $2u_3\Omega_1$ is neglected in Eq. (11). However, the terms $\frac{u_3}{h_3}\frac{\partial u_2}{\partial x_3}$ and $2u_3\Omega_1$

may be relevant close to the stagnation point because $u_3 \approx ||\mathbf{u}||$ and $\Omega_1 \approx ||\mathbf{\Omega}||$. Therefore, Eq. (10) should be valid only after

145 a slightly downstream distance from the stagnation point. Moving all terms except the one containing $\frac{\partial u_2}{\partial x_1}$ to the right-hand side, dividing both sides of the equation by $\rho \frac{u_1}{h_1}$, and including the scale factors given by Eq. (5) yield

$$\frac{\partial u_2}{\partial x_1} = \frac{h_1}{\rho u_1} \left(-\frac{\partial p}{\partial x_2} + F_{rot_2} + \rho u_1^2 \frac{\partial h_1}{\partial x_2} \right). \tag{12}$$

All terms on the right-hand side are known except for the x_2 pressure gradient. An approximation for this term can be found by rewriting the definition of the pressure coefficient with the reference speed equals to the rotational one, i.e.,

$$p = c_p \frac{1}{2} \rho (\omega r_0)^2 + p_\infty, \tag{13}$$

150 and assuming that

$$c_p = c_{p_0} \frac{r^2}{r_0^2} \frac{\alpha}{\alpha_0}, \tag{14}$$

where c_{p_0} is the pressure coefficient at the radial position r_0 and $r = x_2 + r_0$. Equation (14) models the variation in c_p due to the change of the reference velocity with r, as well as a first-order variation in c_p due to the change of the angle of attack α. The latter is defined as

155 $$\alpha = \tan^{-1} \left(\frac{w_\infty}{\omega r_0} \right) + \theta (x_2), \tag{15}$$

with w_∞ and θ representing the incoming-flow velocity and the geometric twist angle, respectively. Note that Eq. (14) is singular for $\alpha_0 = 0$ and may not be very accurate for small values of α_0. Therefore, some other approximations may be more suitable for these cases. With inspiration from the conical-wing approximation (Cebeci, 1999; Sturdza, 2003), c_{p_0} is assumed to be constant along conical lines. These lines as well as other parameters related to the conical-wing approximation are illustrated
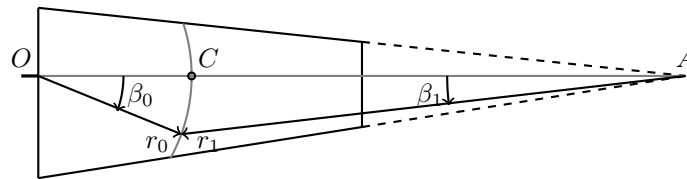
160 in Fig. 2.

Figure 2. Conical parameters. O and A are the center of rotation and the cone apex, respectively. Lines of constant β_1 are the conical lines.

With this assumption, the derivative of c_{p_0} in the x_2 direction can be related to its derivative in the x_1 direction by

$$\frac{\partial c_{p_0}}{\partial x_2} = -\tan (\beta_1 + \beta_0) \frac{\partial c_{p_0}}{\partial x_1}. \tag{16}$$

WIND ENERGY SCIENCE DISCUSSIONS

The angles β_1 and β_0 are defined as

$$\beta_1 = \sin^{-1}\left(\frac{x_{1_c} - x_1}{r_1}\right), \quad \beta_0 = \sin^{-1}\left(\frac{x_{1_c} - x_1}{r_0}\right), \tag{17}$$

165 where x_{1_c} denotes the x_1 coordinate of point C, where the line connecting the center of rotation O and the cone apex A intersects the arc with radius r_0. These assumptions lead to an expression for the pressure derivative, given by

$$\frac{\partial c_p}{\partial x_2} = -\tan\left(\beta_1 + \beta_0\right)\frac{\partial c_{p_0}}{\partial x_1}\frac{r^2}{r_0^2}\frac{\alpha}{\alpha_0} + c_{p_0}\left(\frac{\alpha}{\alpha_0}\frac{2r}{r_0^2} + \frac{r^2}{r_0^2}\frac{1}{\alpha_0}\frac{\partial \alpha}{\partial x_2}\right). \tag{18}$$

Inserting Eqs. (13), (14), and (18) in Eq. (12) provides an expression that can be integrated along x_1 to obtain the distribution of u_{2_e} in this direction. However, it is necessary to obtain an approximation for u_{2_e} at the initial point of integration. In order

170 to do that, we use as inspiration the swept-wing approximation (Cebeci, 1999) and assume that u_{2_e} can be approximated by the velocity over a conical line (see Fig. 2). This approximation yields

$$u_{2_e} = (2\omega r_0 - u_{1_e})\tan\left(\beta_1 + \beta_0\right), \tag{19}$$

where $2\omega r_0$ is a reference velocity. However, Eq. (19) is not very accurate if u_{1_e} is small, as is the case near the attachment line. As such, it is advisable to start the integration at a position x_{1_0} downstream of the attachment line, where u_{1_e} has a value

175 that is comparable to the freestream velocity. An approximate initial value for u_{2_e} at the corresponding x_{1_0} location can be found from

$$u_{2_e}(x_{1_0}) = [2\omega r_0 - u_{1_e}(x_{1_0})](x_{1_c} - x_{1_0})\frac{r_0 + r_1}{r_0 r_1}. \tag{20}$$

3   PSE model

The coordinate system employed in the PSE analysis is the one in Fig. 1. The PSE is derived from the continuity, Navier-Stokes,

180 energy, and state equations (Hanifi et al., 1994; Kundu et al., 2016), as shown in Eqs. (21) to (24). Because of the complexity of performing a full three-dimensional analysis, periodicity is assumed in the x_2 direction. Moreover, rotation terms are added to the momentum equations.

$$\frac{\partial \rho}{\partial t} + \nabla \cdot (\rho \mathbf{u}) = 0, \tag{21}$$

185
$$\rho \left[\frac{\partial \mathbf{u}}{\partial t} + (\mathbf{u} \cdot \nabla) \mathbf{u} \right] = -\nabla p + \frac{1}{Re} \nabla \left[\lambda (\nabla \cdot \mathbf{u}) \right] + \frac{1}{Re} \nabla \cdot \left[\mu \left(\nabla \mathbf{u} + \nabla \mathbf{u}^T \right) \right] + \mathbf{F_{rot}}, \tag{22}$$

$$\rho c_p \left[\frac{\partial T}{\partial t} + (\mathbf{u} \cdot \nabla) T \right] = \frac{1}{RePr} \nabla \cdot (\kappa \nabla T) + (\gamma - 1) \frac{M^2}{Re} \left[(\mathbf{u} \cdot \nabla) p \, \Phi \right], \tag{23}$$

$$\gamma M^2 p = \rho T, \tag{24}$$

190

$$\mathbf{F_{rot}} = -\rho \left[2\mathbf{\Omega} \times \mathbf{u} + \mathbf{\Omega} \times (\mathbf{\Omega} \times \mathbf{x}) \right], \tag{25}$$

$$\Phi = \lambda (\nabla \cdot \mathbf{u})^2 + \frac{1}{2} \mu \left(\nabla \mathbf{u} + \nabla \mathbf{u}^T \right)^2, \tag{26}$$

where $\lambda = -\frac{2}{3} \mu$ denotes the second viscosity coefficient under the Stokes hypothesis. The quantities in these equations have
195 been normalized with the reference values given in Table 1, with l_0 selected as the local boundary-layer thickness $\left(\frac{\mu_\infty x_1}{\rho_\infty u_\infty} \right)^{\frac{1}{2}}$.
The curvature terms are evaluated numerically using standard geometrical relations (Råde and Westergren, 2004).

The flow can be decomposed as

$$\mathbf{q}(x_1, x_3, t) = \bar{\mathbf{q}}(x_1, x_3) + \tilde{\mathbf{q}}(x_1, x_3, t), \tag{27}$$

where t denotes time, $\bar{\mathbf{q}} = \left(\bar{u}_1, \bar{u}_2, \bar{u}_3, \bar{T}, \bar{\rho} \right)^T$ stands for the vector of variables of the base-flow from the BL model or the
200 mean-flow from RANS (assumed $\mathcal{O}(1)$), and $\tilde{\mathbf{q}}$ is the vector of the perturbation of these variables (assumed $\mathcal{O}(\epsilon)$) (Hanifi
et al., 1994). The perturbation part has the form

$$\tilde{\mathbf{q}}(x_1, x_3, t) = \hat{\mathbf{q}}(x_1, x_3) e^{i\Theta}, \tag{28}$$

where $\hat{\mathbf{q}}(x_1, x_3)$ denotes the slowly varying part of the perturbation, i the imaginary unit, and Θ is found from

$$\Theta = \int_0^{x_1} \alpha(x') \, dx' + \beta x_2 - \gamma t, \tag{29}$$

205 where α and β are the wavenumber in the x_1 and x_2 directions, respectively, whereas γ denotes the temporal angular frequency
of the disturbance. Including these relations in Eqs. (21) to (24), assuming that the variation in the x_1 direction is weak

compared to the variation in the x_3 one (there is a scale of $1/Re$ between them), neglecting terms of order ϵ^2, and collecting terms that are multiplied by $\hat{\mathbf{q}}, \frac{\partial \hat{\mathbf{q}}}{\partial x_3}, \frac{\partial^2 \hat{\mathbf{q}}}{\partial x_3^2}, \frac{\partial \hat{\mathbf{q}}}{\partial x_1}$, respectively, into matrices $\mathbf{B_1}, \mathbf{B_2}, \mathbf{B_3}, \mathbf{B_4}$, we obtain a system of the form

$$\mathbf{B_1}\hat{\mathbf{q}} + \mathbf{B_2}\frac{\partial \hat{\mathbf{q}}}{\partial x_3} + \mathbf{B_3}\frac{\partial^2 \hat{\mathbf{q}}}{\partial x_3^2} + \mathbf{B_4}\frac{\partial \hat{\mathbf{q}}}{\partial x_1} = \mathbf{0}. \tag{30}$$

210   Equation (30) can be rewritten as an equivalent first-order system given by

$$\mathbf{C_1}\hat{\mathbf{r}} + \mathbf{C_2}\frac{\partial \hat{\mathbf{r}}}{\partial x_3} + \mathbf{C_3}\frac{\partial \hat{\mathbf{r}}}{\partial x_1} = \mathbf{0}, \tag{31}$$

with $\hat{\mathbf{r}}$ being a vector consisting of the amplitude function $\hat{\mathbf{q}}$ and its derivatives in the x_3 direction (Hanifi et al., 1994). The computer algebra software Maple (Maplesoft, 2016) is used to obtain Eq. (31). In addition, the following normalization condition is used

$$215 \quad \int_0^\infty \hat{\mathbf{q}}^* \frac{\partial \hat{\mathbf{q}}}{\partial x_3} dx_3 = 0, \tag{32}$$

where the superscript $*$ denotes the complex conjugate (Hanifi et al., 1994). The following boundary conditions are employed

$$\begin{cases} \hat{u}_1 = \hat{u}_2 = \hat{u}_3 = \hat{T} = 0, & \text{for } x_3 = 0, \\ \hat{u}_1, \hat{u}_2, \hat{u}_3, \hat{T} \to 0, & \text{for } x_3 \to \infty. \end{cases} \tag{33}$$

The derivatives in the x_3 direction are computed with a fourth-order compact finite-difference scheme, whereas the derivatives in the x_1 direction are computed with a second-order compact finite-difference scheme. Given initial values of α and β, 220   the growth of the disturbances along x_1 is evaluated by marching Eq. (31) in the x_1 direction. In order to avoid restrictions on the step size, the stabilization method described in Andersson et al. (1998) is employed.

4   Results

The accuracy of the proposed quasi-three-dimensional edge velocity, BL, and PSE models is investigated by comparison with results from the EllipSys3D RANS code (Michelsen, 1992, 1994; Sørensen, 1994, 2009). This solver is based on the 225   incompressible Navier-Stokes equations and employs a block-structured, finite-volume discretization, including a second-order upwind scheme for the discretization of convective terms and a central difference scheme for the discretization of the viscous ones. Turbulence is modeled using the SST $k - \omega$ turbulence model (Menter, 1993) and transition predictions are performed using a database method combined with a model for the turbulence intermittency factor γ (Michelsen, 1992, 1994; Sørensen, 1994, 2009).

230   Two different full-scale wind-turbine rotors are investigated. Both have three blades, and their geometries are illustrated in Fig. 3. The shaded colors show a normalized measure of the axial position of each mesh point on the blade surface. The first geometry (Geometry 1) has a tapered and twisted blade with a symmetric NACA 63-018 airfoil profile along its entire span. It was mainly designed to allow the investigation of the accuracy of the conical-wing-based edge velocity model when applied to a geometry respecting its geometrical assumptions. The second geometry (Geometry 2) has a tapered and twisted blade with

235   spanwise-varying cross-sectional properties. This enables the evaluation of the quasi-three-dimensional model when applied to a general wind-turbine blade geometry. It is assumed that the flows over the three blades are similar so that it is sufficient to analyze one blade. We focus on the suction side of the blade since transition often occurs earlier there.

(a) Geometry 1   (b) Geometry 2
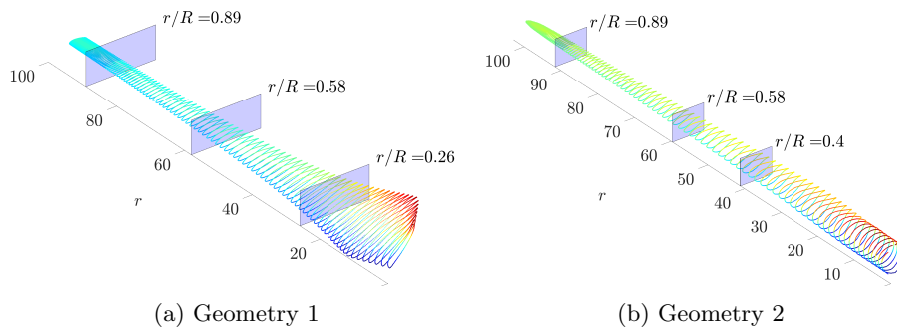
Figure 3. Wind-turbine blades with radial sections of analysis. The surface is colored with a normalized measure of the axial position of the mesh point. The radial coordinate r is given in meters. R is the radius of the wind-turbine rotor.

The main parameters of the two cases are given in Table 2. Both were computed using a temperature of 287.5 K, density of $1.225 \, \mathrm{kg \cdot m^{-3}}$, dynamic viscosity of $1.784 \cdot 10^{-5} \, \mathrm{kg \cdot m^{-1} \cdot s^{-1}}$, ratio of specific heats of 1.4, and gas constant of

240    $287 \, \mathrm{J \cdot kg^{-1} \cdot K^{-1}}$. The meshes used for the RANS computations of Geometries 1 and 2 have $15.5 \cdot 10^6$ nodes, of which $118 \cdot 10^3$ are surface ones. The boundary layer is discretized with approximately 50 nodes in the wall-normal direction. The corresponding meshes for the BL and PSE models have 200 and 500 points in this direction, respectively. This level of discretization provided spatially converged results for test cases. However, a lower number of grid points could be used for increased performance when computing the envelope of N factors with the PSE.

245 **4.1 Spanwise edge velocity**

In this section, we compare the chordwise distributions of spanwise velocity at the edge of the boundary layer obtained with numerical simulations and the edge velocity model (EVM). The streamwise velocity at the inviscid streamline u_{1_e} required as input to the EVM is obtained from RANS and XFOIL simulations. Then, EVMR and EVMX refer to the EVM results with inputs from RANS and XFOIL, respectively. The analyses are performed in the inner ($0 < r_0/R \leq 1/3$), middle ($1/3 <$

250    $r_0/R \leq 2/3$), and outer ($2/3 < r_0/R \leq 1$) parts of the blade, where r_0 is the radial position of analysis and R is the radius of the wind-turbine rotor.

Table 2. Physical parameters of the wind turbines.

	Geometry 1	Geometry 2
Number of blades	3	3
Radius [m]	100.0	102.9
Position of maximum chord [m]	12.0	30.0
Root chord [m]	7.5	5.4
Tip chord [m]	3.7	2.9
Maximum chord [m]	14.2	6.0
Root twist angle [°]	-90.0	0.0
Tip twist angle [°]	0.0	-4.0
Twist angle at position of maximum chord [°]	-17.0	-11.3
Blade cross section (airfoil profile)	NACA 63-018	Varying
Rotational velocity [$\mathrm{rad \cdot s^{-1}}$]	0.64	0.90
Horizontal free stream velocity [$\mathrm{m \cdot s^{-1}}$]	8.0	10.0
Tip-speed ratio	8.0	9.3
Average chord Reynolds number	$1.48 \cdot 10^7$	$1.55 \cdot 10^7$

Figure 4 presents the results for Geometry 1 with u_{2_e} being nondimensionalized by the freestream velocity. One can observe that the spanwise velocity is of the order of 1 % of the freestream velocity, except close to the stagnation point, where it can reach higher values. After 10 % of the chord, the EVMR results agree with those from RANS for the middle and outer radial

255　locations. The differences between the EVMX and RANS results are also small for these sites. They are related to the fact that the c_p distributions from XFOIL are approximations for those from RANS. More important discrepancies between the EVM and RANS results occur close to the stagnation point and at the inner radial position. The reason is that the approximation for the pressure gradient in the x_2 direction (Eq. (16)) is more accurate for higher radii and chordwise positions. The underlying hypothesis that the c_p does not vary over conical lines may not be respected close to the root of the blade and stagnation

260　point because of changes in the airfoil geometry and flow three-dimensionality. The latter is supported by the higher spanwise velocities found at $r_0/R = 0.26$ and in the vicinities of the stagnation point. Moreover, the ratio u_2/u_1 becomes even more important at lower radii since u_1 tends to be smaller.

The results for Geometry 2 are presented in Fig. 5. The maximum chord of the blade occurs at $r_0/R = 0.3$, where the EVM is not supposed to work. Thus, $r_0/R = 0.40$ is selected as the inner radial location. At this coordinate, both the EVMR and

265　EVMX indicate a higher spanwise velocity than RANS. The agreement improves for increasing radial and chordwise positions. In particular, the EVMR results are close to the RANS ones after 15 % of the chord at $r_0/R = 0.58$ and 0.89. The differences between EVMX and EVMR results, which result from the mismatch between the c_p distributions from XFOIL and RANS, are small. The discrepancies at the inner radial position and close to the stagnation point are due to the non-respect of the conical-
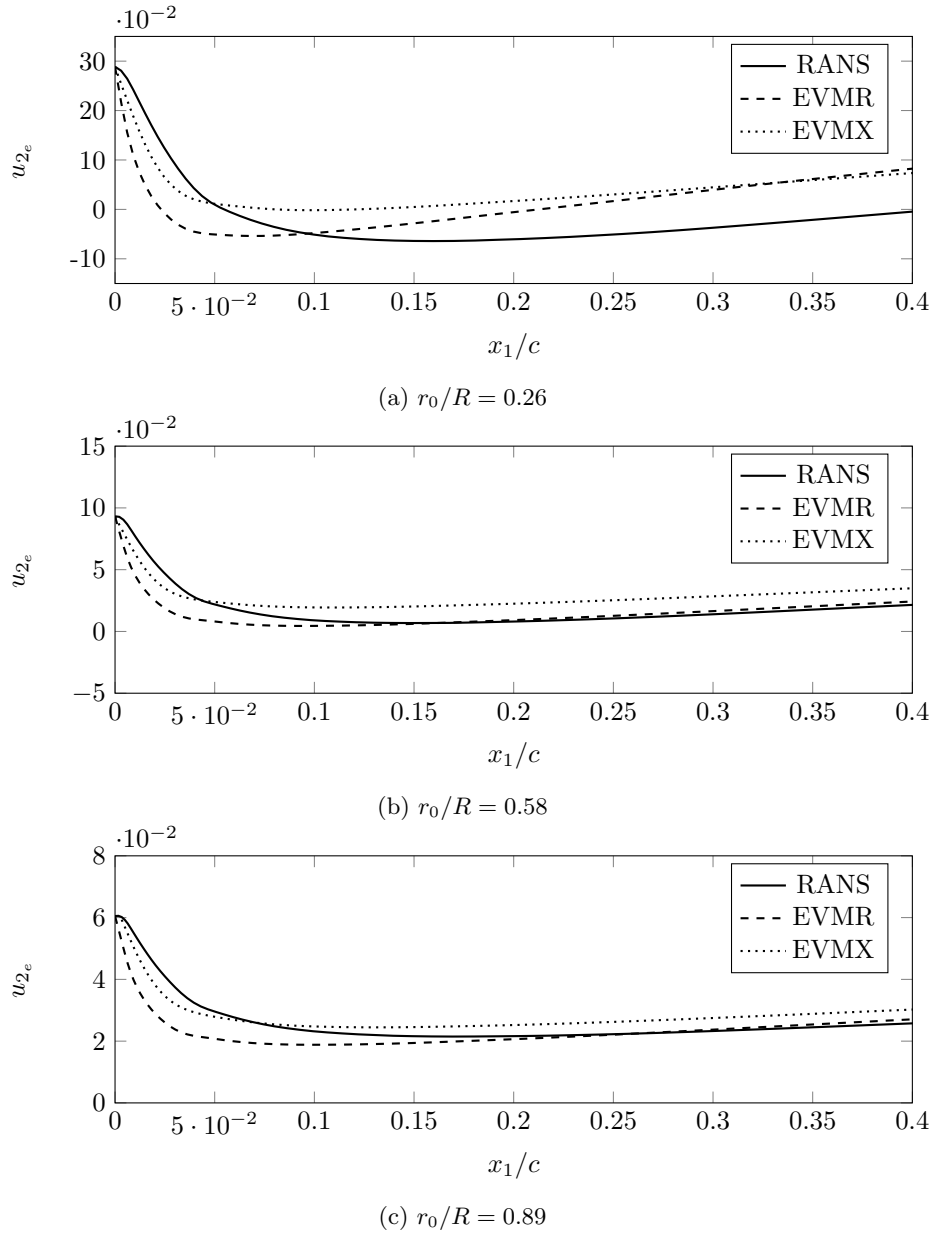
(a) $r_0/R = 0.26$

(b) $r_0/R = 0.58$

(c) $r_0/R = 0.89$

Figure 4. Spanwise edge velocity for Geometry 1.

line approximation at these locations. More important differences were expected for Geometry 2 since the airfoil variation
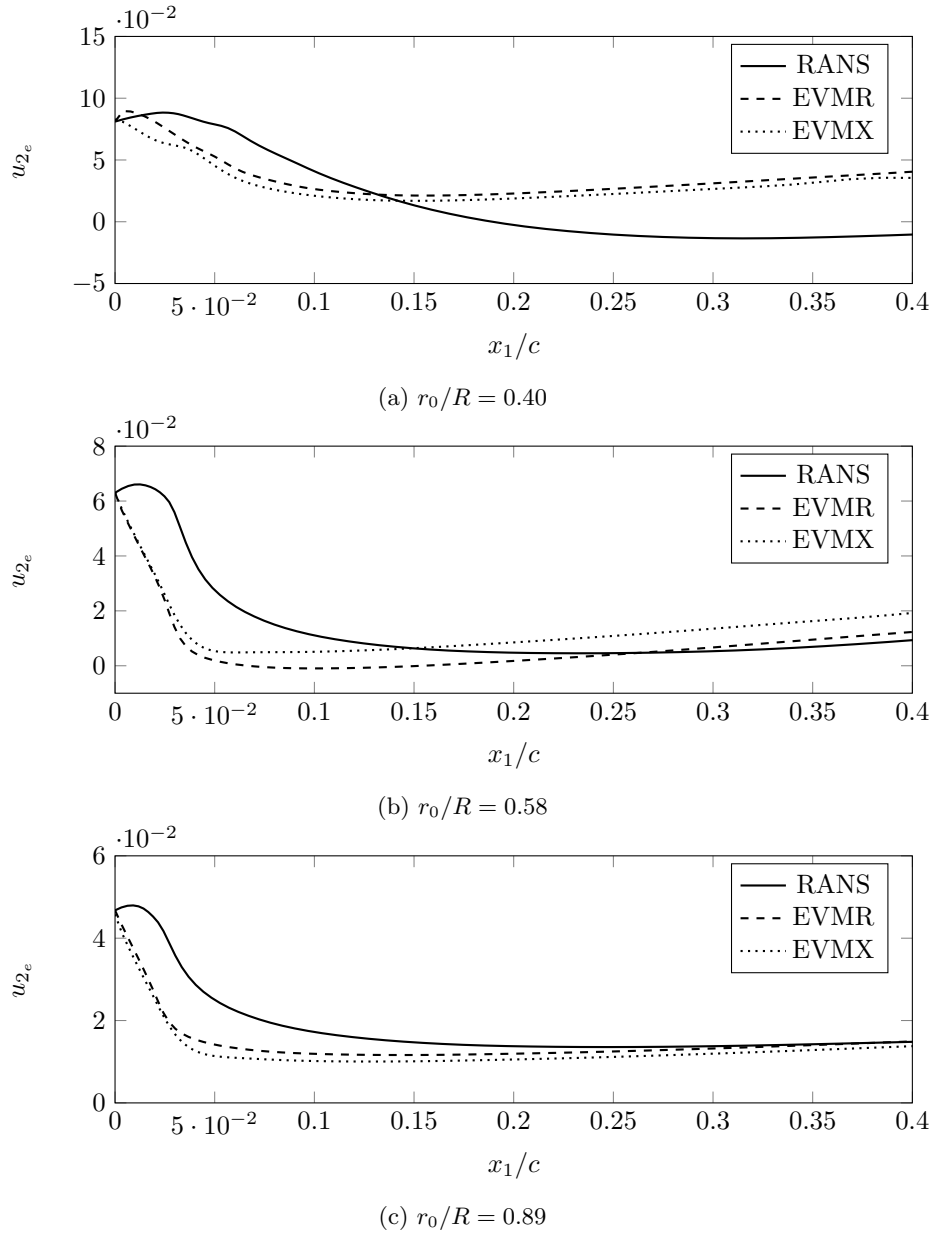along the span spurs changes in the c_p along conical lines.

13

(a) $r_0/R = 0.40$

(b) $r_0/R = 0.58$

(c) $r_0/R = 0.89$

Figure 5. Spanwise edge velocity for Geometry 2.

These results suggest that the edge velocity model can provide a reliable approximation for u_{2_e} for radial positions not too close to the root of the blade and stagnation point. The results are expected to be more accurate for geometries respecting the swept-wing approximation, such as Geometry 1.

4.2 Velocity profiles

275 The streamwise and spanwise velocity profiles for Geometry 1, obtained from RANS and the proposed model, are shown in Fig. 6. Two chordwise positions are analyzed for each radial location. The BLR acronym stands for the BL model with u_{1_e} from RANS and u_{2_e} from EVMR, while BLX refers to this model with u_{1_e} from XFOIL and u_{2_e} from EVMX. The BLR 2D case refers to the base-flow obtained with the two-dimensional BL equations using u_{1_e} from RANS. This model disregards the variations and the velocity in the x_2 direction.

280 Considering Geometry 1, in Fig. 6, we observe that the BLR, BLX, and BLR 2D profiles of streamwise velocity obtained with the boundary-layer equations are in close agreement with the RANS data for all locations. Concerning the spanwise velocity, we note, from Figs. 6a and 6b, that the flow is directed towards the root of the blade at the inner radial position. This reverse flow supports the hypothesis of a considerable three-dimensionality at radial locations closer to the root of the blade (Du and Selig, 2000). Although exhibiting higher values, the BLR and BLX profiles of spanwise velocity present the same 285 shape of those from RANS.

For the middle radial position, as presented in Figs. 6c and 6d, we observe that the BLR profiles of spanwise velocity are in close agreement with those from RANS, whereas the BLX results show higher values of u_2. This is a consequence of the u_{2_e} predicted by the EVMX model being higher than that from RANS. Figures 6e and 6f show that, at the outer radial position, there is close agreement between BLR and RANS results. The BLX results for u_2 display higher values than the BLR and 290 RANS profiles, but the same shape.

Figure 7 presents the results for Geometry 2. We can note that the streamwise velocity profiles obtained with the boundary-layer equations are in close agreement with the RANS results for all positions. Concerning the spanwise velocity at the inner radial location, Figs. 7a and 7b show that the RANS profile presents an inversion of the direction between 10 % and 20 % of the chord. This is similar to what was observed in Geometry 1 and may indicate the three-dimensional character of the flow at 295 lower radii.

Considering the middle radial location, in Figs. 7c and 7d, the BLR and RANS profiles of spanwise velocity are close to each other, and their agreement improves from 15 % to 25 % of the chord. The remaining differences between them at 25 % of the chord are small and can be attributed to the quasi-three-dimensional approach adopted in the BL model. The BLX profile of spanwise velocity displays larger values than that from RANS because of the higher u_{2_e} obtained with the EVMX model. 300 At the outer radial position, as shown by Figs. 7e and 7f, the BLR and RANS results are in close agreement, whereas the BLX results indicate a higher spanwise velocity but the same shape of the profiles compared to the RANS data.

The results show that the BL model accurately predicts the profiles of streamwise velocity. Concerning the spanwise velocity, the agreement between the model and RANS profiles improves with the radial position. The disagreements are larger at the inner radial location, probably because of the influence of three-dimensionality generated by the root of the blade. The results 305 are more accurate for Geometry 1 since it better agrees with the conical-wing approximation and has a constant airfoil geometry. The XFOIL-based results present a higher spanwise velocity than those from RANS. However, this ensues from the higher u_{2_e}
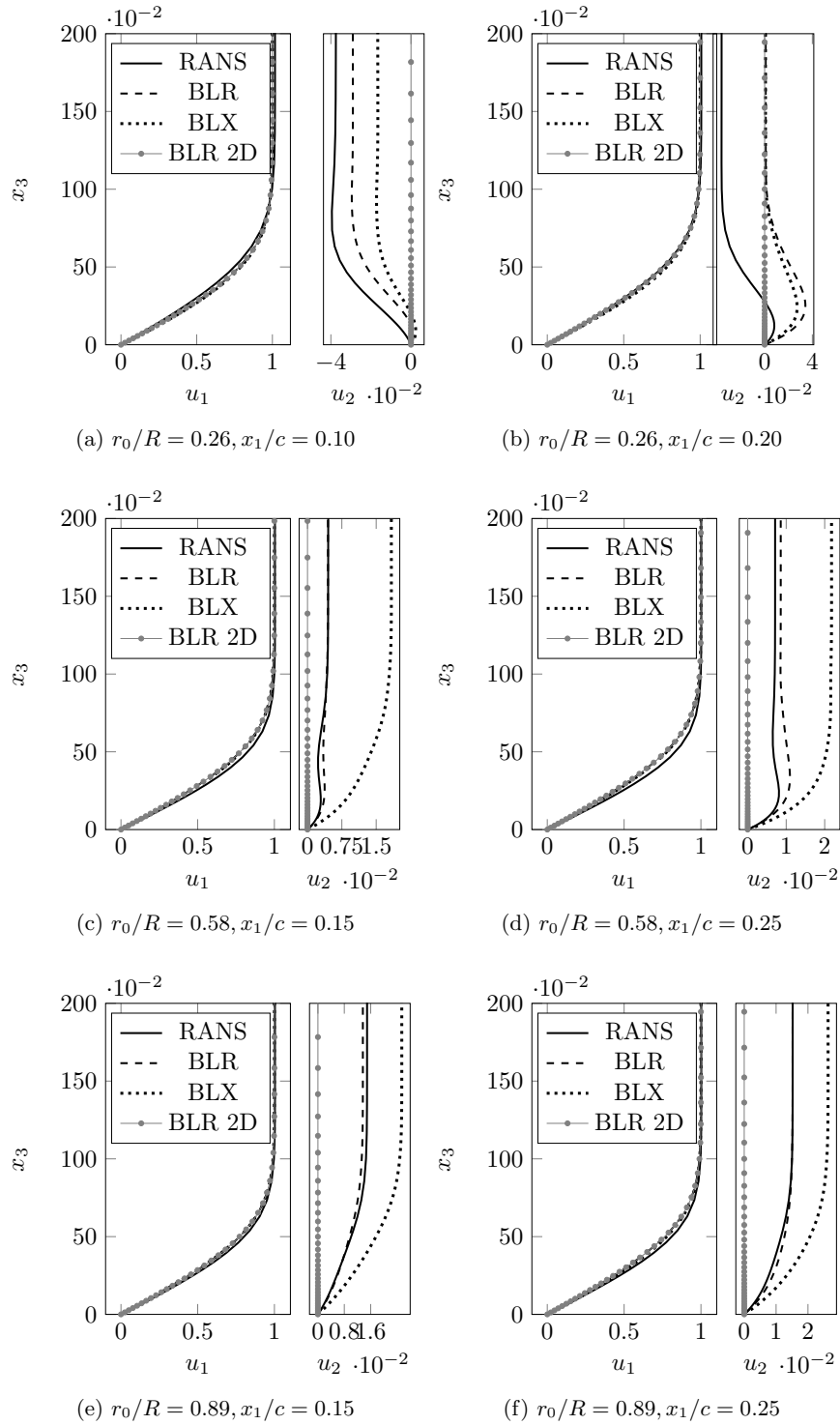
15

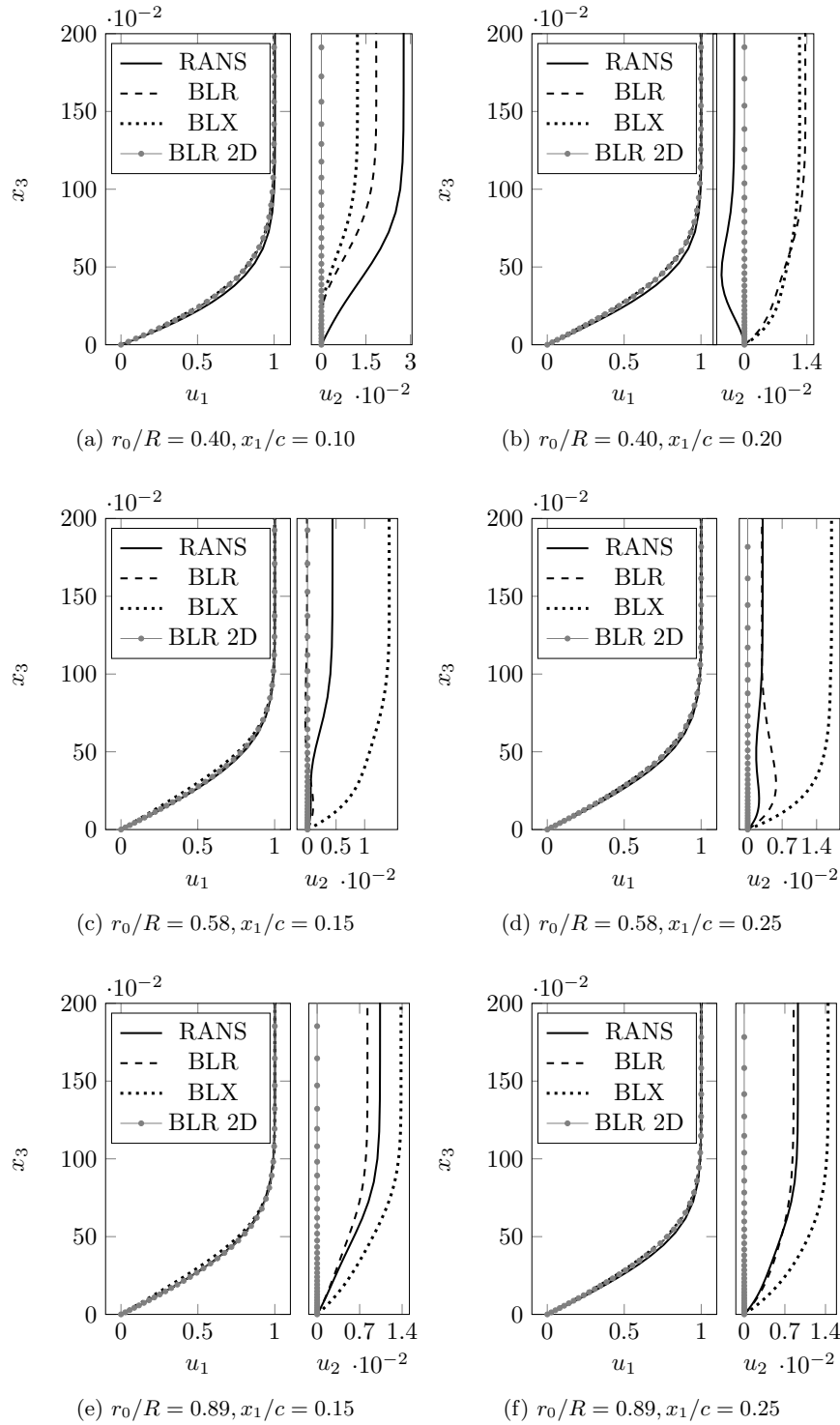**Figure 6.** Boundary layer profiles for Geometry 1.

Figure 7. Boundary layer profiles for Geometry 2.

values obtained with the EVMX model, due to differences in the c_p distributions, and not from the BL model. The magnitude of the spanwise velocity is low, which might indicate a small influence on transition.

We investigate the effects of rotation on the spanwise velocity. Analysis of the EVMX data for Geometry 1 shows that the inviscid streamline is accelerated in the $-x_2$ direction near the stagnation point due to a negative x_2 pressure gradient and the Coriolis force to a lesser extent. The dominant term of the latter is $-2\rho u_1 \Omega_3$ in Eq. (11), pointing in the $-x_2$ direction. After roughly 10 % of the chord, where the flow reaches its maximum streamwise velocity (fully developed flow), the spanwise pressure gradient vanishes. Hence, the centrifugal force, with leading term $\rho\Omega_3^2 x_2$ in Eq. (11), and the inertial term with ρu_1^2 in Eq. (12) overcome the Coriolis force and accelerate the flow in the $+x_2$ direction. For low radii, the Coriolis force tends to increase faster with the rotation speed than the centrifugal and inertial ones, impelling the flow in the $-x_2$ direction. For the middle and outer parts of the blade, the centrifugal and inertial forces tend to grow faster with ω, forcing the flow in the $+x_2$ direction.

Figure 8 presents the profiles of spanwise velocity obtained with the BLX approach at several rotation speeds for Geometry 1. The selected speeds are 5 %, 50 %, 100 %, and 150 % of that used in RANS ($0.64 \, \mathrm{rad \cdot s^{-1}}$). One can observe that, compared to an almost translatoric situation ($0.032 \, \mathrm{rad \cdot s^{-1}}$), rotation tends to accelerate the flow in the x_2 direction, driven by the centrifugal and inertial forces. At the inner radial position, the spanwise velocity decreases for ω rising from 0.32 to $0.96 \, \mathrm{rad \cdot s^{-1}}$ because the Coriolis force grows faster than its counterparts. Considering $r_0/R = 0.58$ and 0.89, the spanwise velocity increases with ω since the centrifugal and inertial forces have higher growth rates for larger radii.

The same analysis is carried out for Geometry 2, for which the rotation speed used in RANS is $0.9 \, \mathrm{rad \cdot s^{-1}}$, and the results are presented in Fig. 9. The airfoils of Geometry 2 sustain negative streamwise and spanwise pressure gradients over a larger chordwise extent compared to Geometry 1. Therefore, it is not possible to decouple a region where the pressure gradient is dominant from another in which rotation effects are preponderant. This fact makes the effects of rotation less clear than in the previous geometry. However, one can still observe the trend described in the theoretical analysis. The flow accelerates with ω in the $-x_2$ and $+x_2$ directions at the inner and outer radial locations, respectively, considering the downstream chordwise stations. At $r_0/R = 0.58$, the increase in the rotation speed tends to accelerate the flow in the $-x_2$ direction, indicating the preponderance of the pressure gradient and Coriolis forces over the inertial and centrifugal ones. This trend remains for the downstream chordwise station (25 % of the chord) since the pressure gradient, pointing in the $-x_2$ direction, does not vanish.

4.3 Transition

The quasi-three-dimensional PSE model is applied to analyze the disturbance growth within the boundary layer. The stability analyses are performed with BLR 2D, BLR, BLX, and RANS base-flows. These analyses will be referred to as PSER 2D, PSER, PSEX, and PSE RANS. Transition is assumed to occur when the amplification factor N based on the integral disturbance energy (Hanifi et al., 1994) reaches N_{crit}. It is assumed $N_{crit} = 9$ in the current work. In the EllipSys3D code, used to perform the RANS simulations, the intermittency factor γ is zero in the laminar region and one in the fully turbulent flow. γ starts to grow when the database method embedded in the solver indicates that transition occurs. Therefore, it is reasonable to select

WIND
ENERGY
SCIENCE
DISCUSSIONS
Open Access
eawe
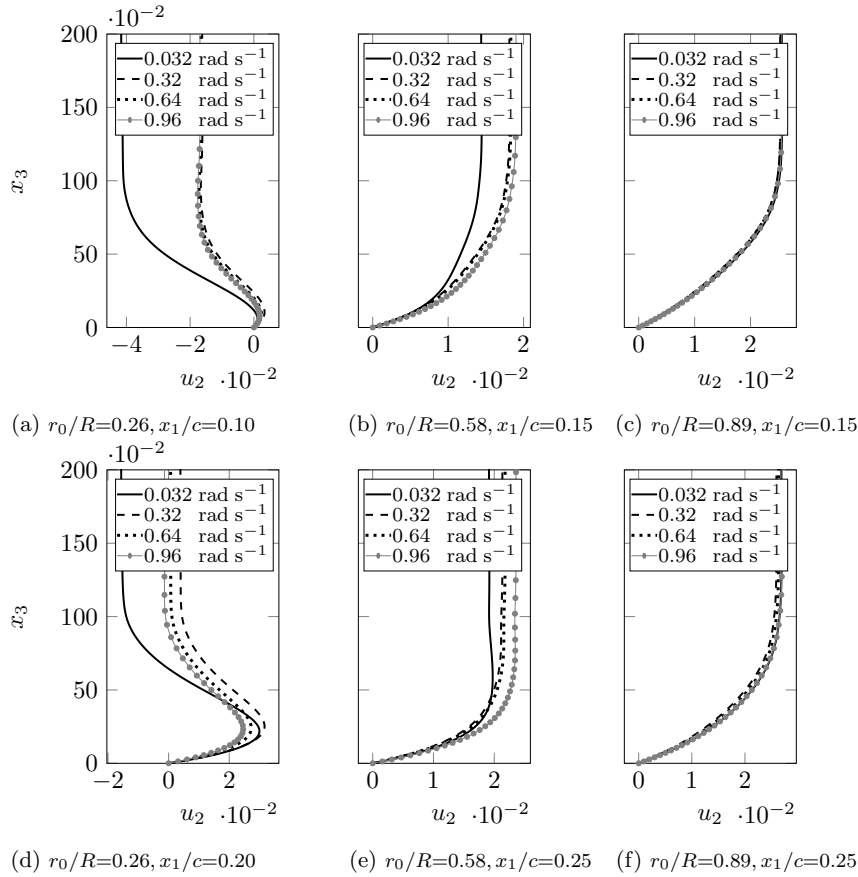european academy of wind energy

Figure 8. Spanwise velocity profiles for Geometry 1 for several rotation speeds.

a small value for this parameter to indicate the transition location, and $\gamma = 0.01$ is selected. These results are referred to as RANS ($\gamma = 0.01$).

The transition locations as a function of the radial position are presented in Fig. 10 for Geometry 1. The results indicate that transition is delayed as the radial position increases. This is in agreement with observations from the literature that report stabilization effects of rotation for increasing radii (Du and Selig, 2000). At the inner part of the blade, up to $r_0/R = 0.40$, PSER and RANS transition locations are close to each other. For the middle and outer parts, the RANS database method indicates earlier transition locations than the PSER results with a maximum difference of 10 % at $r_0/R = 0.89$. Moreover, the RANS and the PSER 2D results are close to each other, which possibly indicates that the RANS transition locations disregard stabilizing effects of three-dimensionality and are thus overly premature. The PSE RANS results (not shown) support this claim because they presented only modes that do not reach N_{crit}. This fact means that the RANS base-flow becomes turbulent (stable) too early, before a mode could reach N_{crit}. The later transition locations obtained with the PSER approach seem to be a consequence of the stabilization provided by considering the velocity and gradients in the spanwise direction. The PSEX
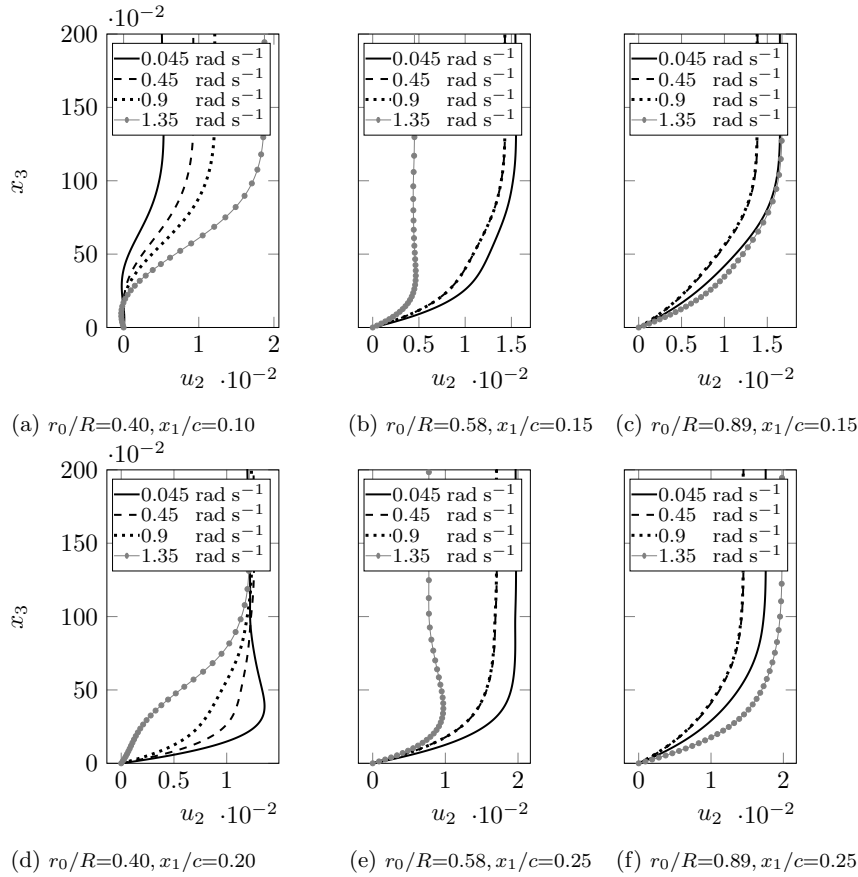
Figure 9. Spanwise velocity profiles for Geometry 2 for several rotation speeds.

results indicate transition locations generally lying between those from the PSER and RANS. These differences arise from the pressure distributions from XFOIL not exactly matching those from RANS, although they are close to each other. The maximum difference between the PSEX and PSER results is 12 % at $r_0/R = 0.26$.

Figure 11 presents the transition locations for Geometry 2. The PSER and PSEX results are close to each other and indicate later onsets of transition than the other methods. The maximum difference between PSER and RANS transition locations is 27 % at $r_0/R = 0.40$. The discrepancies between PSER and PSEX results occur because the pressure distributions from XFOIL do not exactly reproduce those from RANS despite being close to each other. The RANS and PSER 2D transition locations lie near one another and indicate earlier transition onsets. It is possible to infer that RANS converges to a two-dimensional transition mechanism and that the three-dimensionality, as considered in the PSER and PSEX results, has a stabilizing effect. The fact that the PSE RANS results (not shown) presented no mode reaching N_{crit} also supports the claim that transition is triggered too early in RANS and the validity of the later PSER and PSEX transition locations. The increase in the radial

position has the effect of delaying the transition onset. However, this effect is less marked in Geometry 2 because the relative importance of the rotation effects compared to the spanwise pressure gradient is smaller.
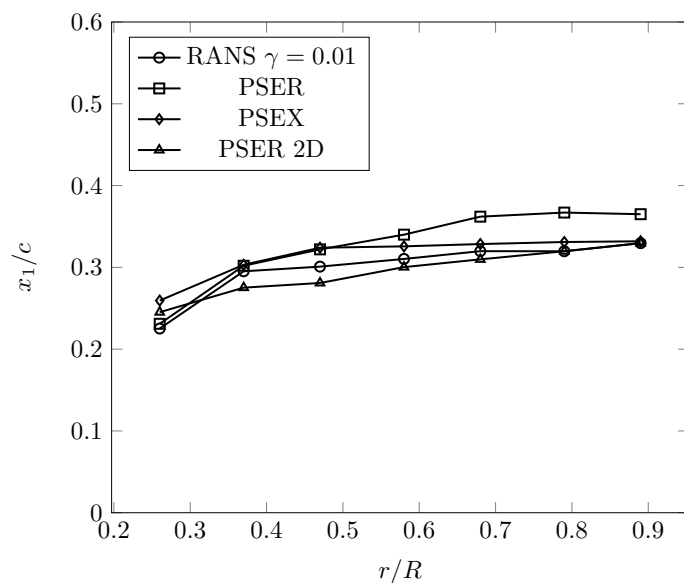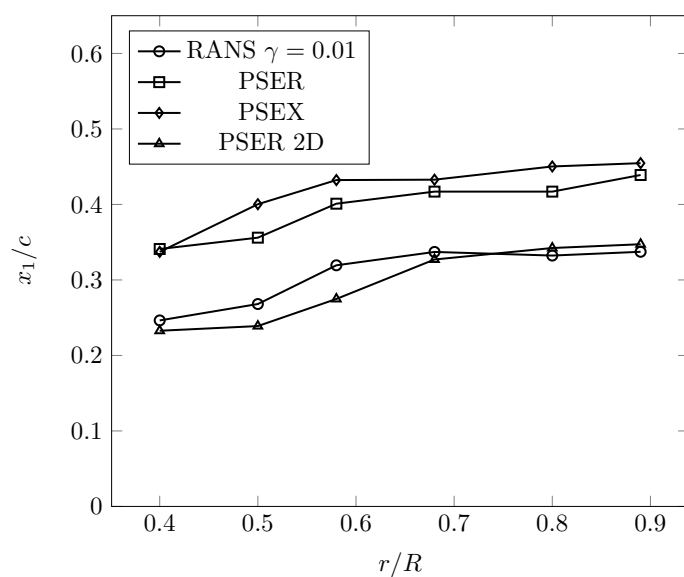

Figure 10. Transition locations for Geometry 1.

Figure 11. Transition locations for Geometry 2.

365   The PSER contours of N factor as a function of the chordwise position and propagation angle η are shown in Fig. 12 for Geometries 1 and 2. η is the angle between the inviscid streamline and the perturbation propagation direction. The dashed red line indicates the transition location. Considering Geometry 1 in Figs. 12a, 12c, and 12e, we observe that the region of critical N factor is less symmetrical and more displaced towards low η at the inner radial location. The mode causing transition at this location has $\eta = -52°$, whereas its counterparts at the middle and outer radial positions have respectively $\eta = -34°$ and $-10°$.

370   This behavior may be linked to the higher spanwise velocity at $r_0/R = 0.26$, which allows the occurrence of transition via more oblique waves. Moreover, transition occurs significantly earlier at $r_0/R = 0.26$ ($x_1/c = 0.23$) compared to $r_0/R = 0.58$ and 0.89 ($x_1/c = 0.34$ and 0.37, respectively).

    Regarding Geometry 2 in Figs. 12b, 12d, and 12f, the critical regions are more spread along the η direction, showing the susceptibility of transition to a broader range of waves compared to Geometry 1. At the middle and outer radial locations,

375   the modes causing transition present respectively $\eta = -30°$ and $-11°$, close to those indicated by Geometry 1. However, at the inner radial location, transition occurs with $\eta = -6°$, which is higher than the angle obtained for the first geometry. The reason is possibly the lower spanwise velocity of Geometry 2. The contours also show that the increase in the radius shrinks the critical region and delays transition.

    Figure 13 presents the profiles of the perturbation of u_1 velocity of the modes leading to transition in Geometry 1. At the

380   inner radial position, the PSER and PSEX modes are in close agreement, indicating that the transition mechanisms computed by them are the same. There are differences between the modes close to the wall at the middle and outer radial positions. These differences probably ensue from the higher spanwise velocity in the base-flow of the PSEX analyses. The modes resemble Tollmien-Schlichting (TS) waves. However, the modes tend to have a single-peaked structure at $r_0/R = 0.26$, associated with their high propagation angle (in absolute value).

385   The results for Geometry 2 are presented in Fig. 14. There are differences between the modes in the vicinities of the airfoil for the inner and middle radial locations. These variations are probably caused by the spanwise velocity, which is higher in the base-flow of the PSEX analyses. At the outer radial position, the PSER and PSEX modes converge since the spanwise velocity profiles are closer to each other. The modes causing transition in Geometry 2 also bear a resemblance to TS waves.

    In the next, we analyze the effects of rotation on the transition location. Figure 15 presents the PSEX transition locations

390   as a function of the radial position and rotation speed for Geometry 1. The analyses were performed with rotation speeds corresponding to 5 %, 50 %, 100 %, and 150 % of that from RANS for Geometry 1 ($0.64\,\mathrm{rad\cdot s^{-1}}$). The trend shown in the picture indicates that the increase in the rotation speed accelerates transition. In particular, the rise in ω from 0.32 to $0.96\,\mathrm{rad\cdot s^{-1}}$ makes transition occur 37 % earlier. The fact that the case corresponding to 5 % of the RANS rotation speed (not shown) did not present any mode reaching N_{crit} further indicates the destabilizing effect of rotation. These effects take place

395   through the rotation terms in the PSE and the variation of the spanwise velocity. The former seems to be preponderant since, at $r_0/R = 0.89$, there is no significant variation in the spanwise velocity with ω, but transition occurs earlier regardless. There is a delay in transition for increasing radius up to $r_0/R = 0.47$. In this region, the Coriolis force is prevalent. Further increases in radius do not produce significant changes in the transition locations, indicating a balance between the rotation effects.
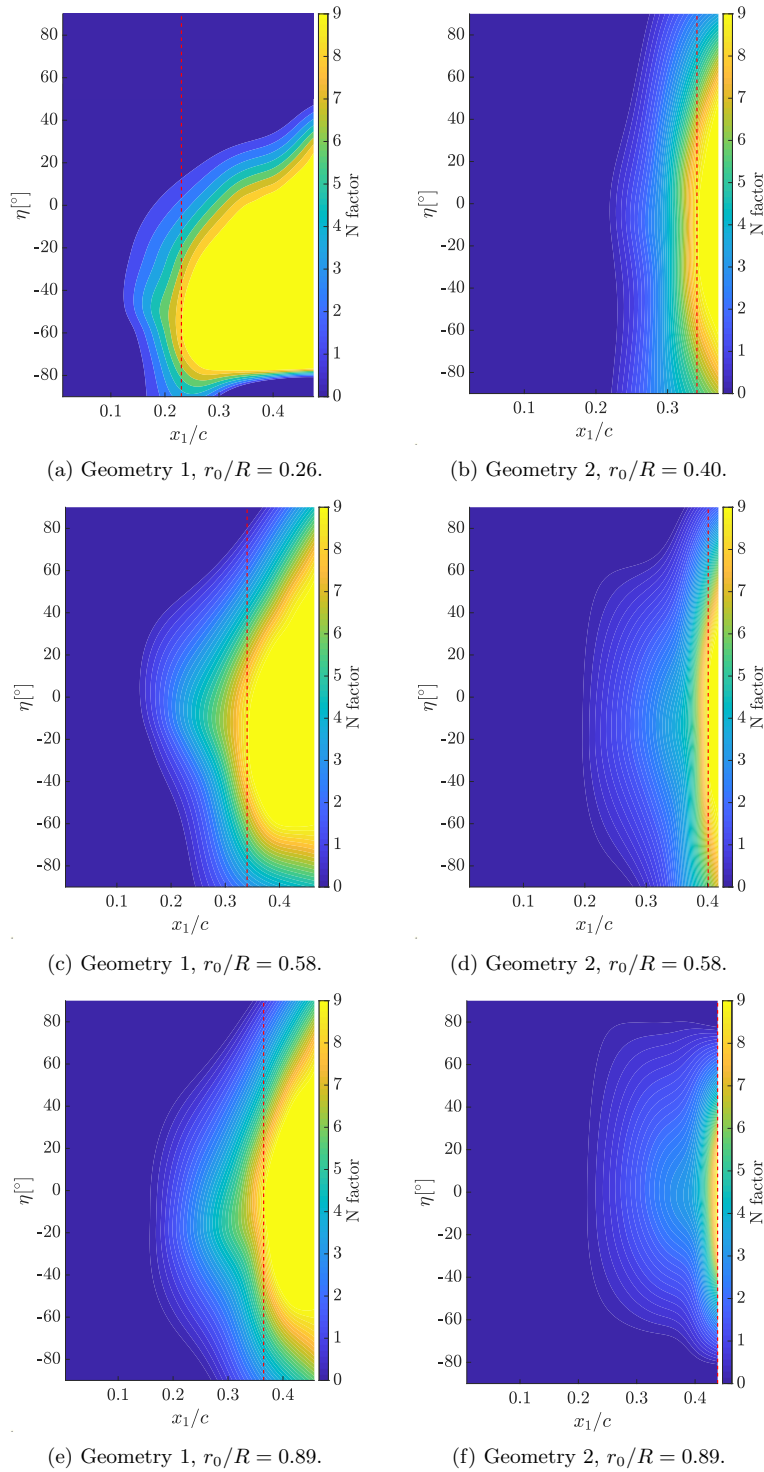
(a) Geometry 1, $r_0/R = 0.26$.

(b) Geometry 2, $r_0/R = 0.40$.

(c) Geometry 1, $r_0/R = 0.58$.

(d) Geometry 2, $r_0/R = 0.58$.

(e) Geometry 1, $r_0/R = 0.89$.

(f) Geometry 2, $r_0/R = 0.89$.

Figure 12. N-factor contours from PSER for three radial positions.

WIND
ENERGY
SCIENCE
DISCUSSIONS

(a) $r_0/R = 0.26$ (b) $r_0/R = 0.58$ (c) $r_0/R = 0.89$
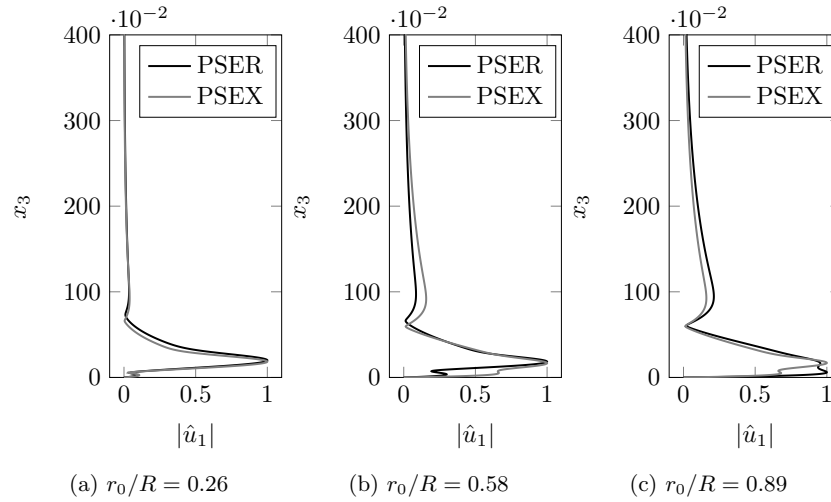
Figure 13. PSE results for the mode leading to transition in Geometry 1.

(a) $r_0/R = 0.40$ (b) $r_0/R = 0.58$ (c) $r_0/R = 0.89$
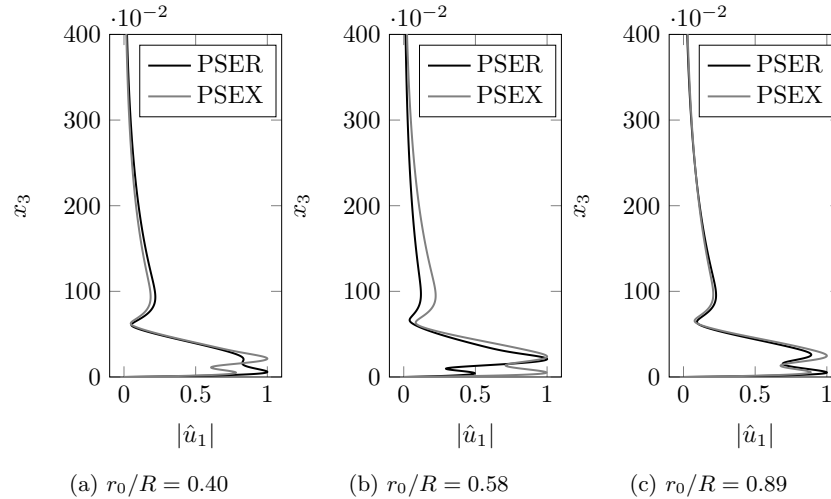
Figure 14. PSE results for the mode leading to transition in Geometry 2.

Figure 16 portrays the results for Geometry 2. The increase in the rotation speed plays a destabilizing role. This observation
is supported by the fact that the case with 5 % of the RANS rotation speed (not shown) presented no mode reaching N_{crit}.
However, the variation of ω does not play a role as important as for Geometry 1. For instance, transition occurs 8 % earlier
on average for an increase in ω from 0.45 to 1.35 rad $\cdot$ s^{-1}. The smaller sensitivity of transition to variations in the rotation
speed ensues from the fact that the airfoils of Geometry 2 maintain favorable pressure gradients over a larger chordwise extent,
which makes the rotation effects have smaller relative importance. Although the changes in the spanwise velocity with the
rotation speed may affect the transition locations, the rotation effects embedded in the PSE seem to be the driving force of

the variation in the transition onsets. This is because the spanwise velocity of Geometry 2, especially at the middle and outer radial locations, varies more with the rotation velocity than in Geometry 1, but the transition locations present smaller changes. Transition is delayed when increasing the radius up to $r_0/R = 0.58$, a range along which the Coriolis force is dominant. Only slight variations in the transition locations occur after this radial position, pointing to a balance in the rotation effects.
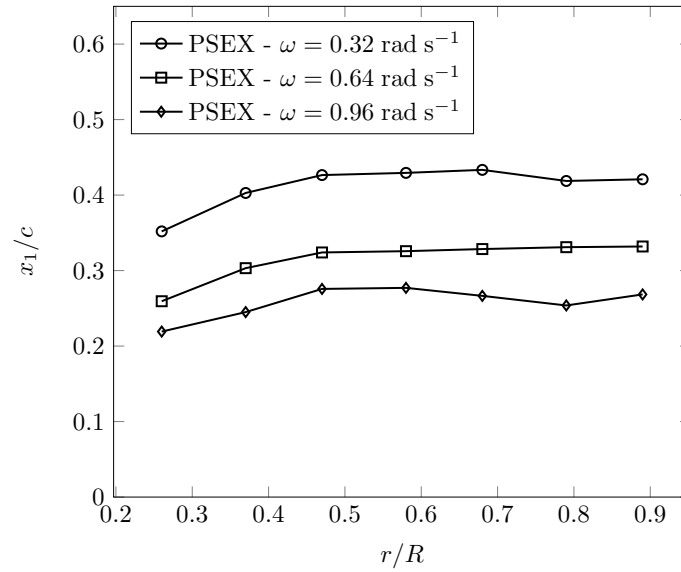
Figure 15. Transition locations for Geometry 1 for several rotation speeds.
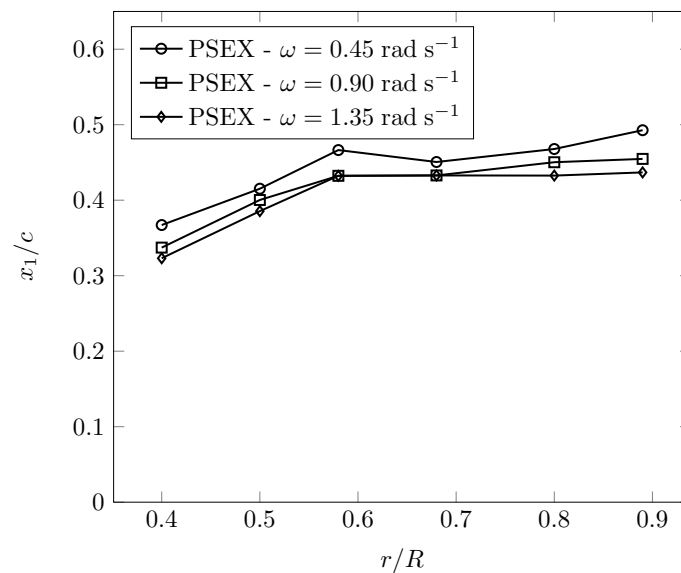

Figure 16. Transition locations for Geometry 2 for several rotation speeds.

410 The PSEX contours of N factor at $r_0/R = 0.58$ for Geometries 1 and 2 are shown in Fig. 17. In the case of Geometry 1, as shown in Figs. 17a, 17c, and 17e, the increase in the rotation speed forces the critical region towards lower chordwise positions. This region lies mostly in the $-\eta$ half-plane, meaning that the waves causing transition propagate in the $-x_2$ direction (towards the root of the blade). These modes present $\eta = -27°$, $-20°$, and $-20°$ for $\omega = 0.32$, 0.64, and 0.96 rad·s^{-1}. Considering Geometry 2, in Figs. 17b, 17d, and 17f, we also observe the displacement of the critical region to lower x_1/c with the increase

415 in ω. Moreover, the flat critical region extending from $\eta = -60°$ to $40°$ obtained with $\omega = 1.35$ rad·s^{-1} shows that the higher rotation velocity allows transition to be triggered by a broader range of disturbances. The critical region is located mostly in the $-\eta$ half-plane, indicating stronger susceptibility of transition to waves traveling towards the root of the blade. The modes causing transition present $\eta = -7°$, $-15°$, and $-28°$ for $\omega = 0.45$, 0.9, and 1.35 rad·s^{-1}. The analysis of the full geometry indicates that the increase in ω reduces the critical $|\eta|$ in the region $0 \leq r_0/R \leq r$, where $r = 0.58$ and 0.5 for Geometries 1

420 and 2. After this position, the opposite occurs, i.e., rising ω leads to increasingly oblique critical modes. This inference is in agreement with the observation of earlier transition at lower radii, since modes with smaller $|\eta|$, tending to two-dimensional waves, have a tendency to be more unstable.

The PSEX profiles of the modes leading to transition in Geometry 1 are displayed in Fig. 18. The variable being plotted is the disturbance in the streamwise velocity. All modes collapse at the inner radial location, indicating that the change in

425 ω does not alter the transition mechanism. At $r_0/R = 0.58$ and 0.89, the modes for $\omega = 0.64$ and 0.96 rad·s^{-1} are in close agreement, while the mode for $\omega = 0.32$ rad·s^{-1} differs from the previous ones mainly close to the wall. The shape of the modes seems to be closely related to their propagation angles, with higher $|\eta|$ modes tending to have only one peak like those at $r_0/R = 0.26$. Figure 19 shows the results for Geometry 2. At the inner radial location, the modes for $\omega = 0.9$ and 1.35 rad·s^{-1} are in agreement except close to the wall. The mode for $\omega = 0.45$ rad·s^{-1} has a single-peaked structure and is

430 associate with a high $|\eta|$. At $r_0/R = 0.58$, the modes for $\omega = 0.45$ and 0.9 rad·s^{-1} have double peaks and agree, whereas the one for $\omega = 1.35$ rad·s^{-1} does not present a pronounced peak close to the wall since its associated $|\eta|$ is high. At the outer radial location, the modes present similar shapes and propagation angles. The critical modes in the two geometries resemble TS waves. The single-peaked modes observed at $r_0/R = 0.26$ for Geometry 1 and $r_0/R = 0.40$ for Geometry 2 ($\omega = 0.45$ rad·s^{-1}) might represent an intermediate stage between a TS and crossflow transition. These modes have $\eta \leq -50°$, and the spanwise

435 velocity reaches its highest values at these locations.

5 Conclusions

A framework for transition prediction applicable to wind-turbine rotors comprising a model for the base-flow and a version of the PSE is developed. The technique accounts for quasi-three-dimensional and rotational effects. It aims at providing more reliable transition predictions than database methods at a computational cost lower than those requiring three-dimensional

440 simulations. This work also analyzes the role of three-dimensionality and rotation on the transition onset.

The developed method provides accurate profiles of streamwise velocity, and, for locations not too close to the root of the blade and stagnation point, spanwise velocity. The use of c_p distributions from XFOIL as input to the model leads to an
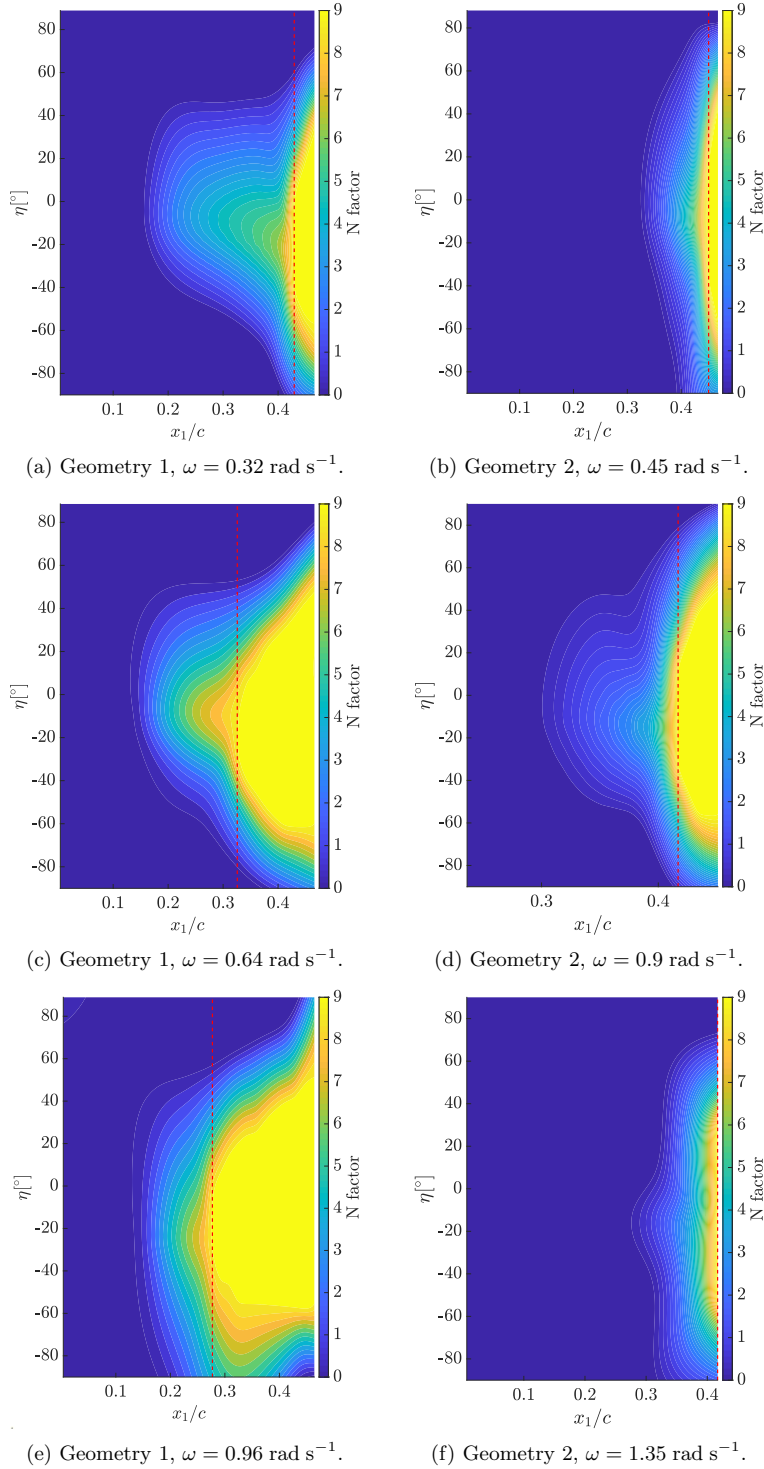
(a) Geometry 1, $\omega = 0.32$ rad s^{-1}.

(b) Geometry 2, $\omega = 0.45$ rad s^{-1}.

(c) Geometry 1, $\omega = 0.64$ rad s^{-1}.

(d) Geometry 2, $\omega = 0.9$ rad s^{-1}.

(e) Geometry 1, $\omega = 0.96$ rad s^{-1}.

(f) Geometry 2, $\omega = 1.35$ rad s^{-1}.

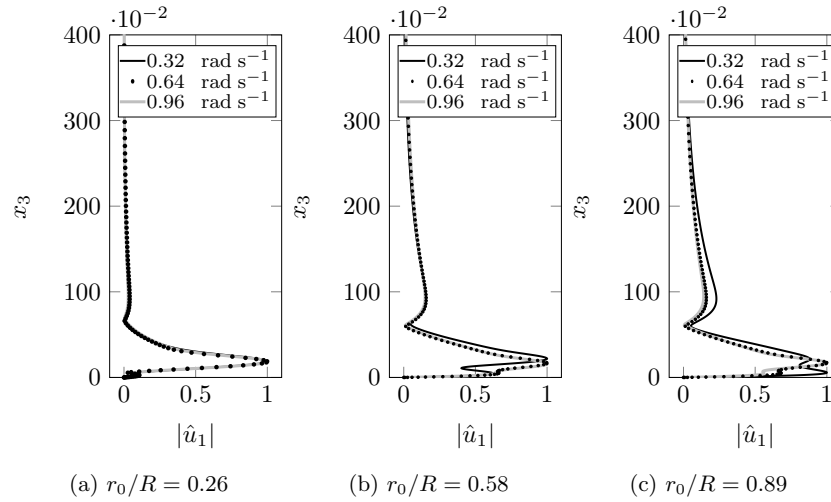**Figure 17.** N-factor contours from PSEX at $r_0/R = 0.58$ for several rotation speeds.

Figure 18. PSEX results for the mode leading to transition in Geometry 1 for several rotation speeds.
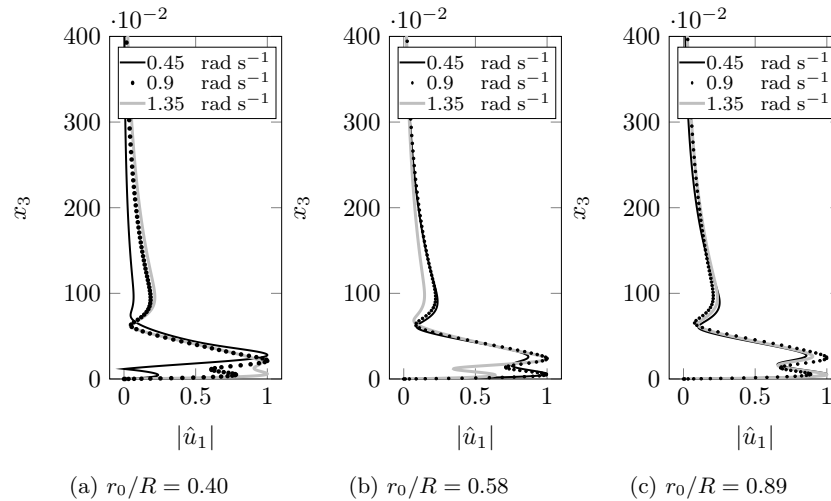

Figure 19. PSEX results for the mode leading to transition in Geometry 2 for several rotation speeds.

overestimation of the spanwise velocity. The discrepancies diminish for higher radial positions. The analysis of the rotational effects reveals that they accelerate the flow towards the tip of the blade in the developed flow region and towards the root close
445   to the stagnation point.

Regarding the transition onset, three-dimensionality displays a stabilizing role. The quasi-three-dimensional effects considered in the developed model, such as the velocity and gradients in the spanwise direction, delay transition. This is true even though the spanwise velocity has a low magnitude in most of the blade. Conversely, considering a two-dimensional base-flow leads to earlier transition locations. These results are close to those from the database method in the EllipSys3D RANS code,

450   indicating that the latter predicts forward transition locations. PSE analyses of the RANS base-flow corroborate this result,
       showing that transition is triggered in RANS before a mode has sufficiently amplified.

       Rotation plays a destabilizing role, hastening the onset of transition. Moreover, airfoils with a smaller region of favorable
       pressure gradient are more susceptible to rotational effects. Transition seems to be caused by TS waves. However, at low radii,
       where the spanwise velocity reaches higher values, the critical modes are more oblique and present a distinctive shape that
455   points to the possibility of them being intermediates between TS and crossflow modes.

       Despite overestimating the spanwise velocity, the use of XFOIL input in the developed model leads to transition locations
       close to those obtained with RANS input. Therefore, the model fulfills the goal of providing a reliable estimate for the transition
       onset without requiring three-dimensional simulations.

Code and data availability. Part of the codes and data employed/developed is available upon direct request with the corresponding author.

460   *Author contributions.* TF implemented the models, performed the analysis, and wrote the final version of the manuscript. ML developed
       the model, obtained part of the results, and wrote the first version of the document. NS and FZ performed the RANS simulations using
       the EllipSys3D code. AH and DH developed the NOLOT PSE code (among other researchers), supported the analysis, provided useful
       discussions, and contributed with critical feedback. All authors reviewed the manuscript.

Competing interests. The authors declare that they have no conflict of interest.

References

Andersson, P., Henningsson, D. S., and Hanifi, A.: On a stabilization procedure for the parabolic stability equations, J ENG MATH, pp. 311–332, https://doi.org/10.1023/A:1004367704897, 1998.

Cebeci, T.: An engineering approach to the calculation of aerodynamic flows, Springer, 1 edn., 1999.

Colonia, S., Leble, V., Steijl, R., and Barakos, G.: Assessment and Calibration of the γ-Equation Transition Model at Low Mach, AIAA J, 55, 1126–1139, https://doi.org/10.2514/1.J055403, 2017.

Drela, M.: XFOIL: An analysis and design system for low Reynolds number airfoils, in: Lecture Notes in Engineering, vol. 54, Springer-Verlag, 1989.

Drela, M.: Three-Dimensional Integral Boundary Layer Formulation for General Configurations, in: Proceedings of the 21st AIAA Computational Fluid Dynamics Conference, San Diego, California, 24-27 June, 2013, 2013.

Du, Z. and Selig, M. S.: The effect of rotation on the boundary layer of a wind turbine blade, RENEW ENERG, 20, 167–181, https://doi.org/10.1016/S0960-1481(99)00109-3, 2000.

Dumitrescu, H. and Cardos, V.: Inboard Stall Delay Due to Rotation, in: Fundamental and Advanced Topics in Wind Power, edited by Carriveau, R., chap. 3, IntechOpen, Rijeka, Croatia, https://doi.org/10.5772/18632, 2011.

Garcia, N. R., Sørensen, J. N., and Shen, W. Z.: A quasi-3D viscous-inviscid interaction code: Q^3UIC, J PHYS CONF SER, 555, 012 041, https://doi.org/10.1088/1742-6596/555/1/012041, 2014.

Goldstein, S.: On laminar boundary layer flow near a position of separation, Q J MECH APPL MATH, 1, 43–69, https://doi.org/10.1093/qjmam/1.1.43, 1948.

Greenspan, H. P.: The theory of rotating fluids, Cambridge University Press, Cambridge, UK, 1 edn., 1968.

Hanifi, A., Henningson, D. S., Hein, S., Bertolotti, F. P., and Simen, M.: Linear nonlocal Instability Analysis - the linear NOLOT code, Technical report FFA-TN 1994-54, The Aeronautical Research Institute of Sweden, Bromma, Sweden, 1994.

Hernandez, G. G. M.: Laminar-Turbulent transition on Wind Turbines, Ph.D. thesis, Department of Mechanical Engineering, Technical University of Denmark, 2011.

Krumbein, A.: Application of Transition Prediction, in: MEGADESIGN and MegaOpt - German Initiatives for Aerodynamic Simulation and Optimization in Aircraft Design. Notes on Numerical Fluid Mechanics and Multidisciplinary Design, edited by Kroll, N., Schwamborn, D., Becker, K., Rieger, H., and Thiele, F., vol. 107, pp. 107–120, Springer, Berlin, Heidelberg, https://doi.org/10.1007/978-3-642-04093-1_8, 2009.

Kundu, P. K., Cohen, I. M., and Dowling, D. R.: Fluid Mechanics, Academic Press, 6 edn., 2016.

Langtry, R. B., Gola, J., and Menter, F. R.: Predicting 2D Airfoil and 3D Wind Turbine Rotor Performance using a Transition Model for General CFD Codes, in: Proceedings of the 44th AIAA Aerospace Sciences Meeting and Exhibit, Reno, Nevada, 9-12 January 2006, 2006.

Langtry, R. B., Sengupta, K., Yeh, D. T., and Dorgan, A. J.: Extending the $\gamma - Re_{\Theta_t}$ Local Correlation based Transition Model for Crossflow Effects, in: Proceedings of the 45th AIAA Fluid Dynamics Conference, Dallas, Texas, 22-26 June 2015, 2015.

Maplesoft: Maple, version 2016, 2016.

Menter, F.: Zonal Two Equation k-ω Turbulence Models For Aerodynamic Flows, in: Proceedings of the 23rd Fluid Dynamics, Plasmadynamics, and Lasers Conference, Orlando, Florida, 6-9 July, 1993, 1993.

Menter, F. R., Langtry, R., and Völker, S.: Transition Modelling for General Purpose CFD Codes, FLOW TURBUL COMBUST, 95, 277–303, https://doi.org/10.1007/s10494-006-9047-1, 2006.

Menter, F. R., Smirnov, P. E., Liu, T., and Avancha, R.: A One-Equation Local Correlation-Based Transition Model, FLOW TURBUL

505   COMBUST, 77, 583–619, https://doi.org/10.1007/s10494-015-9622-4, 2015.

Michelsen, J.: Basis3D - a Platform for Development of Multiblock PDE Solvers, Technical report AFM 92-05, Technical University of Denmark, 1992.

Michelsen, J.: Block structured Multigrid solution of 2D and 3D elliptic PDE's, Technical Report AFM 94-06, Technical University of Denmark, 1994.

510   Pasquale, D. D., Rona, A., and Garrett, S. J.: A selective review of CFD transition models, in: Proceedings of the 39th AIAA Fluid Dynamics Conference, San Antonio, Texas, 22-25 June, 2009, 2009.

Råde, L. and Westergren, B.: Mathematics Handbook for Science and Engineering, Springer, 5 edn., 2004.

Saric, W. S., Reed, H. L., and White, E. B.: Stability and transition of three-dimensional boundary layers, ANNU REV FLUID MECH, 35, 413–440, https://doi.org/10.1146/annurev.fluid.35.101101.161045, 2003.

515   Schlichting, H. and Gersten, K.: Boundary-Layer Theory, Springer, 9 edn., 2017.

Sturdza, P.: An aerodynamic design method for supersonic natural laminar flow aircraft, Ph.D. thesis, Department of Aeronautics and Astronautics, Stanford University, 2003.

Sørensen, N. N.: General Purpose Flow Solver Applied to Flow over Hills, Technical Report Risø-R- 827-(EN), Risø National Laboratory, Roskilde, Denmark, 1994.

520   Sørensen, N. N.: CFD modeling of Laminar-Turbulent Transition for Airfoils and Rotors using the $\gamma - \tilde{Re}_\Theta$ Model, WIND ENERGY, 12, 715–733, https://doi.org/10.1002/we.325, 2009.

van Garrel, A.: Integral Boundary Layer Methods for Wind Turbine Aerodynamics - A Literature Survey, Technical report ECN-C–04-004, Energy Research Centre of the Netherlands, 2004.

van Ingen, J. L.: The e^N method for transition prediction. Historical review of work at TU Delft, in: Proceedings of the 38th Fluid Dynamics

525   Conference and Exhibit, Seattle, Washington, 23-26 June, 2008, 2008.

Warsi, Z. U. A.: Fluid Dynamics, CRC Press, Boca Raton, Florida, 2 edn., 1999.